Princeton Plasma Physics Laboratory

PPPL- 4324

PPPL- 4324

# Predictive Simulations of ITER Including Neutral Beam Driven Toroidal Rotation

Federico D. Halpern, Arnold H. Kritz, Glenn Bateman, Alexei Y. Pankin,
Robert V. Budny,[2] and Douglas C. McCune

June 2008

Prepared for the U.S. Department of Energy under Contract DE-AC02-76CH03073.

# Princeton Plasma Physics Laboratory
# Report Disclaimers

---

## Full Legal Disclaimer



## Trademark Disclaimer



---

# PPPL Report Availability

## Princeton Plasma Physics Laboratory:

http://www.pppl.gov/techreports.cfm

## Office of Scientific and Technical Information (OSTI):

http://www.osti.gov/bridge

---

**Related Links:**

**U.S. Department of Energy**

**Office of Scientific and Technical Information**

**Fusion Links**

# Predictive simulations of ITER including neutral beam driven toroidal rotation

Federico D. Halpern,[1] Arnold H. Kritz,[1] Glenn Bateman,[1] Alexei Y. Pankin,[1] Robert V. Budny,[2] and Douglas C. McCune[2]
[1]*Department of Physics, Lehigh University, 16 Memorial Drive East, Bethlehem, Pennsylvania 18015, USA*
[2]*Princeton Plasma Physics Laboratory, P. O. Box 451, Princeton, New Jersey 08543, USA*

(Received 26 February 2008; accepted 21 April 2008; published online 10 June 2008)

Predictive simulations of ITER [R. Aymar *et al.*, Plasma Phys. Control. Fusion **44**, 519 (2002)], discharges are carried out for the 15 MA high confinement mode (H-mode) scenario using PTRANSP, the predictive version of the TRANSP code. The thermal and toroidal momentum transport equations are evolved using turbulent and neoclassical transport models. A predictive model is used to compute the temperature and width of the H-mode pedestal. The ITER simulations are carried out for neutral beam injection (NBI) heated plasmas, for ion cyclotron resonant frequency (ICRF) heated plasmas, and for plasmas heated with a mix of NBI and ICRF. It is shown that neutral beam injection drives toroidal rotation that improves the confinement and fusion power production in ITER. The scaling of fusion power with respect to the input power and to the pedestal temperature is studied. It is observed that, in simulations carried out using the momentum transport diffusivity computed using the GLF23 model [R. Waltz *et al.*, Phys. Plasmas **4**, 2482 (1997)], the fusion power increases with increasing injected beam power and central rotation frequency. It is found that the ITER target fusion power of 500 MW is produced with 20 MW of NBI power when the pedestal temperature is 3.5 keV. © *2008 American Institute of Physics*. [DOI: 10.1063/1.2931037]

## I. INTRODUCTION

Simulations of ITER discharges, which have been carried out using a variety of integrated modeling codes (see, for example, Refs. 1–10), have predicted a wide range in the fusion performance for ITER. One of the factors contributing to the prediction of the wide range in ITER performance is the stiffness of the anomalous transport model used in the simulations. (Stiffness refers to the rapid growth of the drift-wave turbulence transport with increasing temperature gradients above a threshold temperature gradient.) Transport driven by drift-wave turbulence, which accounts for most of the anomalous thermal transport observed in present day experiments, has been included in the simulations using different anomalous transport models such as the GLF23,[5,11] MMM95,[12] Weiland,[13] and mixed Bohm/gyro-Bohm[14] transport models.

Previously, simulations of similar discharge scenarios were carried out and compared using different transport models in different integrated modeling codes (see, for example, Refs. 2 and 3). It is demonstrated in Ref. 2 that differences in transport model stiffness could explain the disagreement between results obtained with the XPTOR code,[15] using the GLF23 model, and results obtained with the BALDUR code,[16] using the MMM95 model. However, in general, it is difficult to assess the cause of the wide range of predictions for ITER performance when the simulations are carried out in different transport codes using different transport models, different heating sources, and different models for various physical phenomena. For instance, in Ref. 1, ITER simulations were carried out using the MMM95 transport model in the BALDUR code with prescribed auxiliary heating profiles, but with self-consistently evolving temperature, density, and current profiles. In Ref. 5, ITER simulations were carried out using the GLF23 transport model in the XPTOR code with the same prescribed auxiliary heating profiles used in Ref. 1 but without self-consistently evolving the current density and particle density profiles. In Ref. 4, ITER simulations were carried out using the mixed Bohm/gyro-Bohm transport model in the JETTO code with heating profiles computed with the PENCIL code.[17] Furthermore, as a consequence of the transport model stiffness, different predictions for the fusion performance of ITER are obtained with different models for the temperature at the top of the H-mode pedestal.

A recent predictive simulation study[8] has focused on understanding hybrid and steady-state operating regimes in ITER. In another recent paper,[9] the performance of an ITER inductive H-mode scenario is modeled, with a particular emphasis on variations in auxiliary heating as well as reduced performance regimes. Some of the reduced performance regimes considered in Ref. 9 are plasmas with only hydrogen or only deuterium ions, as well as discharges with reduced toroidal field, heating power, or beam voltage.

In the present work, simulations of 15 MA H-mode discharges are carried out using the GLF23 and MMM95 anomalous transport models in the PTRANSP code, the predictive version of the TRANSP[18] code, which has been validated extensively in the analysis of experimental data. The PTRANSP code is used to compute the evolution of the temperature, toroidal rotation, current density profiles, and fusion performance using a choice of models for the magnetic equilibrium, density, sawtooth oscillations, neoclassical and anomalous transport, and the width and height of the H-mode edge pedestal. Objectives of the present work in-

 

clude direct comparison of ITER simulations obtained using the GLF23 or MMM95 anomalous transport models in the same code and examining the dependence of ITER performance on the source of plasma heating as well as on the choice of model for the width and height of the H-mode edge pedestal.

The models and simulation method used to carry out the predictive ITER simulations using the PTRANSP code are presented in Sec. II. The computation of density profiles is described in Sec. II A, the computation of temperature profiles in Sec. II B; and the computation of the toroidal rotation profile in Sec. II C. In Sec. III, the models and simulation method described in Sec. II are used to predict the fusion performance in ITER under a variety of conditions. In Sec. III A, ITER plasma profiles and fusion performance are predicted in simulations using 30 MW of NBI or 30 MW of ICRF power, and in Sec. III B, the fusion performance of ITER is examined using different mixes of the amount of NBI or RF heating. Transient changes in the plasma profiles caused by sawtooth oscillations are described in Sec. III C, and results associated with different edge pedestal temperatures are presented in Sec. III D.

In Sec. III E, the projected toroidal rotation of ITER in NBI heated discharges is modeled self-consistently with the evolution of the temperature, the helium ash build-up, and the current density. These evolving profiles can affect the neutral beam heating and torque profiles. Although toroidal rotation might significantly affect the performance of ITER, toroidal rotation has received less attention than the effects associated with profile stiffness and pedestal temperature. In tokamak plasmas, the toroidal rotation drives a radial electric field that can stabilize the drift-wave turbulence.[19] Simulations of tokamak discharges, with momentum transport included, have been carried out with the GLF23 model in Ref. 5. In addition, the GLF23 model for toroidal rotation has been tested against experimental data from Joint European Torus[20] (JET) discharges in JETTO simulations, in which the torque was computed using the PENCIL code (see Ref. 21). The toroidal rotation velocity of ITER was modeled in Ref. 7 with the XPTOR code, but the magnetic equilibrium and the torque sources were fixed input quantities. In Sec. IV, the results associated with the ITER simulations described in this paper are summarized.

## II. SIMULATION PROTOCOL AND PREDICTIVE MODELS IN THE PTRANSP CODE

In this section, the protocol for carrying out ITER simulations and some of the predictive models used in the PTRANSP code are briefly described. Simulations are carried out for a 15 MA H-mode discharge scenario that involves a current, density, and magnetic field strength ramp-up during the first 150 s followed by quasisteady-state conditions during the following 350 s. The following plasma parameters remain constant during the quasisteady-state stage of the discharge: Major radius $R=6.20$ m; minor radius $a=2.0$ m; vacuum toroidal magnetic field $B_T=5.3$ T (specified at $R=6.2$ m); total current $I=15$ MA; elongation $\kappa=1.85$, and triangularity $\delta=0.5$, specified at the separatrix.

Relative to the TRANSP analysis code, the PTRANSP code includes enhanced predictive capabilities such as:

- A model to predict the height and width of the H-mode pedestal.
- Upgraded steering capabilities for predictive modeling, so that switches related to predictive modeling can be modified upon simulation abort and restart.
- Implementation of the Porcelli model for sawtooth triggering and profile mixing.[22]
- Implementation of a numerical scheme that improves the numerical stability of the solution of stiff transport equations.
- Upgraded NBI and RF heating and current drive sources. In particular, PTRANSP now includes a source equilibration module that "freezes" the heating and current drives if they have stopped evolving or if they evolve very slowly.
- Upgraded equilibrium solvers.
- Addition of a new Weiland model to compute thermal, particle, and momentum diffusivities due to the ion temperature gradient and trapped electron mode (ITG/TEM) turbulence.
- Computation of toroidal rotation using the toroidal momentum diffusivity predicted by either the GLF23 model or the Weiland model.

Of particular interest for the ITER simulations presented here is the implementation of the pedestal model, which is described in Sec. II B, and the computation of toroidal momentum transport, which is described in Sec. III C.

The magnetic equilibrium is computed using the ESC code.[23] Sawtooth crashes are assumed to occur with a prescribed period of 5 s. The plasma profiles are mixed after every sawtooth crash, using a density matching method that is similar to the typical Kadomtsev mixing criterion,[24] resulting in flat plasma profiles within the sawtooth mixing region. Profile mixing is carried out for the following profiles: electron temperature $T_e$, ion temperature $T_i$, toroidal rotation frequency $\omega_\phi$, electron density $n_e$, ion density $n_k$ (including impurities, minority ions, fast ions, and helium ash), and current density. The evolution of density, temperature, and toroidal rotation profiles are, respectively, described below in Secs. II A–II C.

### A. Computation of density profiles

The electron density profiles are prescribed as a function of time. The prescribed profiles are shown in Fig. 1 at $t=1$ s (dotted line), $t=50$ s (dashed line), $t=100$ s (dash-dotted line), and at $t=150$ s (solid line). The profiles are almost completely flat in the plasma core, with a narrow and steep gradient near the edge. The effective charge is specified as $Z_{\text{eff}}=1.55$. The density of helium-4 nuclei resulting from fusion reactions is evolved using a prescribed anomalous diffusivity and a prescribed convective velocity. The additional impurity is taken to be boron ($Z=5$) with an atomic weight of 10 amu. The density for two hydrogenic species, deuterium and tritium, are obtained from an algorithm that includes enforcing the quasineutrality condition

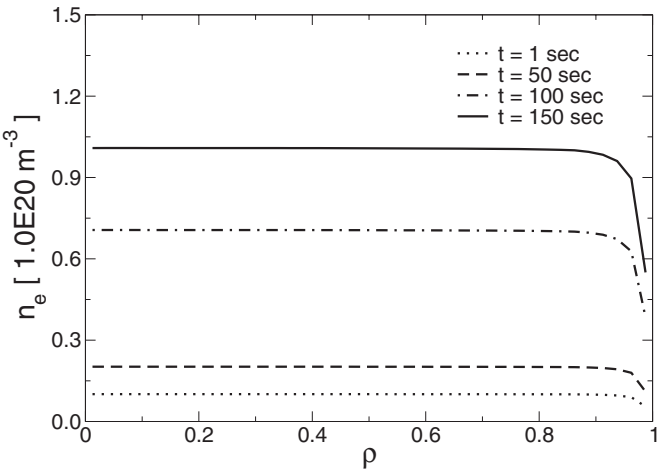


FIG. 1. Electron density profiles are shown as a function of $\rho$ at $t=1$ s (dotted line), $t=50$ s (dashed line), $t=100$ s (dot-dashed line), and $t=150$ s (solid line).

$$n_e = \sum_k Z_k n_k, \tag{1}$$

where $n_e$ is the electron density, $Z_k$ are the ion charges, and $n_k$ are the ion densities. The sum over the ionic densities $n_k$ includes the densities of the main ion species (deuterium and tritium), the density of the helium nuclei, resulting from fusion reactions, as well as the densities of the other nonthermal ions such as the minority ion heating species and fast ions associated with the neutral beam heating.

### B. Computation of temperature profiles

The temperature profiles are evolved self-consistently in PTRANSP using either the MMM95 model or the GLF23 model for anomalous thermal transport, using the NCLASS model for neoclassical transport,[25] and using auxiliary heating and fusion thermal sources. In the simulations, the auxiliary heating power is driven by either ion cyclotron resonant frequency heating (ICRF) or neutral beam injection (NBI) heating. Heating power is injected from 50 to 500 s. The ICRF power deposition profiles are computed using the SPRUCE code,[26] and the NBI power deposition and current drive profiles are computed with the NUBEAM code.[27,28] Deuterium-tritium fusion reactions contribute additional heating power, most of which is absorbed by the electrons. The thermalization of fast alpha particles is computed using a Monte Carlo method with 8000 particles.

The fusion power obtained in the simulations depends primarily on the model used for anomalous thermal transport and on the model used for the pedestal temperature. Since the thermal confinement of H-mode plasma discharges improves with increasing pedestal temperature, the pedestal temperature used as a boundary condition for the temperature profiles is an important factor in predicting the fusion performance of ITER. In Sec. II B 1 below, the procedure used to compute anomalous thermal transport in the simulations is discussed, and in Sec. II B 2, the PEDESTAL module, which is used to compute the width and the temperature at the top of the H-mode pedestal in the ITER simulations, is described.

#### 1. Anomalous thermal transport

The thermal diffusivity due to anomalous transport is computed using either the MMM95 model or the GLF23 model. The MMM95 model is a combination of theory based models. The largest contribution to core thermal transport in the MMM95 model is the transport resulting from the drift-wave turbulence associated with the ion temperature gradient and trapped electron modes (ITG/TEM) as described in the 1995 Weiland model.[12] This model includes physical effects due to finite beta, magnetic shear, electron-ion collisions, impurities, and fast ions.

The GLF23 model[11] computes transport due to ITG, TEM, and electron temperature gradient (ETG) driven turbulence, including physical effects for finite beta, Shafranov shift stabilization, magnetic shear, electron-ion collisions, impurities, and fast ions.

The GLF23 model is derived from nearly the same fundamental fluid equations as the Weiland model, but GLF23 includes a gyro-fluid resonance in the closure of the heat flux equation. The Weiland model and the GLF23 models can be described as critical gradient models, i.e. the drift-wave turbulence drives transport only when the normalized temperature and density gradients increase above a threshold. The effective diffusivity increases rapidly above the threshold, and, therefore, the models are usually described as stiff. The GLF23 and MMM95 models are described in greater detail in Refs. 11 and 12.

In MMM95 and GLF23, the turbulence stabilization effect due to sheared flows is approximated by subtracting the $\mathbf{E}\times\mathbf{B}$ shearing rate $\omega_{\mathbf{E}\times\mathbf{B}}$ from the growth rates of the drift mode instabilities. Sheared flows are driven by the diamagnetic flow, the toroidal flow, and the poloidal flow. In the simulations involving only ICRF heating, the $\mathbf{E}\times\mathbf{B}$ shearing rate due to rotation is associated with only the diamagnetic and poloidal flow since ICRF does not drive toroidal flow in these simulations. The GLF23 model computes the axisymmetric $\omega_{\mathbf{E}\times\mathbf{B}}$ internally, and then multiplies these rates by a calibration constant $\alpha_E=1.35$ (see Refs. 5 and 29). Note that the flux-surface average of $\omega_{\mathbf{E}\times\mathbf{B}}$, which is used in the GLF23 model, can be larger than $\omega_{\mathbf{E}\times\mathbf{B}}$ at the outboard midplane, which are the values used in the MMM95 model.

The thermal diffusivities computed with the MMM95 and GLF23 models are used to evolve the temperature profiles from the magnetic axis to the edge of the plasma. During the H-mode stage of the discharge, the thermal diffusivities are used from the magnetic axis to the top of the edge pedestal. The H-mode pedestal model, which is used to provide the edge boundary condition, is described in the subsection below.

#### 2. Edge pedestal temperature and width

The temperature and width of the H-mode edge pedestal in the ITER simulations are computed using the PEDESTAL module.[30] The width of the pedestal $w_{\mathrm{ped}}$ is determined using a mix of magnetic shear and flow shear and can be expressed as

$$w_{\mathrm{ped}} = C_W \rho_s s^2, \tag{2}$$

where $C_W=2.42$ is a calibration constant, $\rho_s$ is the gyroradius, and $s$ is the magnetic shear $s=(r/q)(dq/dr)$, where $q$ is the magnetic safety factor. Since $q$ is singular at the separatrix, the magnetic shear at the pedestal is estimated using an approximation for $q$ given by

$$q = \left(\frac{0.85a^2 B_T}{IR}\right) \times \left[\frac{[1+\kappa_{95}^2(1+2\delta_{95}^2-1.2\delta_{95}^3)](1.17-0.65a/R)}{[1-(a/R)^2]^2}\right] \times \left\{\left[1+\left(\frac{r}{1.4a}\right)^2\right]^2 + 0.27|[\ln(1-r/a)]|\right\}, \tag{3}$$

where $a$ is the minor radius, $R$ is the major radius, $r$ is the minor radius to the top of the pedestal, $B_T$ is the toroidal magnetic field in tesla, $\kappa_{95}$ is the plasma elongation at $0.95a$, $\delta_{95}$ is the plasma triangularity at $0.95a$, and $I$ is the plasma current in mega-amperes.

The pressure gradient is assumed to be constant in the pedestal region of steep density and temperature gradients. Furthermore, it is assumed that the critical pressure gradient is limited by the first stability limit of the magnetohydrodynamic (MHD) ballooning mode, and consequently related to the critical MHD ballooning parameter $\alpha_c$ by the expression

$$\alpha_c \equiv \frac{2\mu_0 R q^2}{B_T^2}\left(\frac{dp}{dr}\right)_c = 0.4s[1+\kappa_{95}^2(1+5\delta_{95}^2)], \tag{4}$$

where $q$ and $s$ are evaluated using Eq. (3) and its first radial derivative. The pedestal temperature, $T_{\mathrm{ped}}$ is obtained using the relationship $p=nT$ together with Eq. (4):

$$T_{\mathrm{ped}} = 0.323 C_W^2 \left(\frac{B_T}{q^2}\right)^2 \left(\frac{\mu_h}{R^2}\right)\left(\frac{\alpha_c}{n_{\mathrm{ped}}}\right)^2 s^4 \ [\mathrm{keV}], \tag{5}$$

where $\mu_h$ is the average hydrogenic mass in atomic mass units and $n_{\mathrm{ped}}$ is the density at the top of the pedestal in units of $10^{19}$ m$^{-3}$.

In the PTRANSP code, an automated transition between L-mode and H-mode is triggered when the total power exceeds the power threshold[31]

$$P_{\mathrm{TH}} = 2.84 \mu_h^{-1} B_T^{0.82} \bar{n}_{e20}^{0.58} r^{0.81} R \ [\mathrm{MW}], \tag{6}$$

where $\bar{n}_{e20}$ is the line-averaged electron density in units of $10^{20}$ m$^{-3}$. In the ITER simulations, it is found that the power threshold at 100 s is about 40 MW. It is found that L-H transitions can be achieved with as little as 20 MW of auxiliary power, with the rest of the power required to reach the threshold provided by self-heating. A more recent publication[32] predicts $P_{\mathrm{L-H}} \approx 70$ MW at $t=100$ and $\bar{n}_{e20}=0.75$. If this threshold were to be used in the ITER simulations, additional power would be required to reach H-mode and the L-H mode transition would have to be carried out at an earlier stage in the density ramp.

The pedestal width and temperature, computed using Eqs. (2) and (5), are imposed as edge boundary conditions on the temperature profiles after the transition to H-mode occurs. The transition from a low prescribed boundary temperature to the computed pedestal temperature is carried out over several timesteps in order to avoid transient artifacts in the temperature profiles, which could result in numerical instability. Nevertheless, the L-H transition is carried out in only a small fraction of a second, so it is perceived as the sudden transition that is observed in experiments. The radial location of the top of the pedestal is resolved to the nearest grid point in the simulation. The temperature profiles between the top of the pedestal and the plasma edge are approximated as a descending straight line.

When the total power drops to below 75% of the threshold power computed using Eq. (6), PTRANSP reverts to a prescribed edge boundary condition for the temperature profiles. The algorithm used has been designed to allow for an arbitrary number of L-H or H-L transitions, if needed.

### C. Computation of toroidal rotation profiles

Another factor that influences the output fusion power, obtained in the simulations, is the toroidal plasma rotation that drives part of the $\mathbf{E}\times\mathbf{B}$ flow shear. The toroidal rotation frequency is computed using a predictive transport equation that balances toroidal momentum diffusion and convection against torque sources. A derivation of the toroidal momentum transport equation and torque sources used in these simulations can be found in Ref. 33. The neutral beam torque source is computed using the NUBEAM module in the PTRANSP code. The torque sources included in the ITER simulations are: neutral beam driven torques due to the beam collisional force, neutral beam current ($\mathbf{J}\times\mathbf{B}$ torque), beam thermalization, plasma ionization, and charge exchange. Momentum losses due to charge exchange are included. In the plasma core, the beam collisional and $\mathbf{J}\times\mathbf{B}$ torques are dominant. Near the plasma edge, charge exchange losses are dominant. No torque model for the ICRF source is available in the PTRANSP code. Consequently, the toroidal rotation frequency obtained in simulations of ICRF heated discharges is negligible.

In this work, only convective losses due to particle convection across flux surfaces are considered. Note that the GLF23 and MMM95 turbulence models, used to compute the anomalous transport, do not include the effects of turbulence driven momentum convection, which is believed to drive spontaneous rotation in tokamak experiments. The edge toroidal rotation frequency is set to a negligible value (100 rad/s), which might possibly lead to an underestimation of the toroidal momentum confinement.

In the simulations described in Secs. III A–III D, the toroidal momentum diffusivity is taken to be equal to the ion thermal diffusivity; i.e., $\chi_\phi=\chi_i$. In Sec. III E, momentum transport studies are carried out by solving the toroidal momentum transport equation with the toroidal momentum dif-

fusivities computed using the GLF23 model. (Note that the MMM95 model does not include a computation of the toroidal momentum diffusivity.) The neoclassical contribution to toroidal momentum diffusivity is taken to be equal to the neoclassical ion thermal diffusivity. Hence, in Sec. III E the toroidal momentum diffusivity used in the simulations is given by $\chi_\phi = \chi_{\phi,\mathrm{GLF23}} + \chi_{i,\mathrm{NCLASS}}$.

## III. PROJECTED FUSION PERFORMANCE OF ITER

In this section, results obtained in the ITER PTRANSP simulations are described. Of particular interest is the predicted ratio of fusion power to heating power, known as fusion $Q$, which is computed as

$$Q = \frac{P_{\mathrm{DT}}}{P_{\mathrm{NBI}} + P_{\mathrm{ICRF}} + P_{\mathrm{Ohm}}}, \tag{7}$$

where $P_{\mathrm{DT}}$ is the deuterium-tritium fusion reaction power (five times the $\alpha$ power production), $P_{\mathrm{NBI}}$ is the neutral beam heating power, $P_{\mathrm{ICRF}}$ is the ICRF heating power, and $P_{\mathrm{Ohm}}$ is the Ohmic power. To avoid the effects of transients in the heating source profiles, the reported values for $Q$ are time averaged between 480 and 500 s.

The temperature, toroidal rotation frequency, and fusion power are shown in Sec. III A for ITER simulations carried out using 30 MW of heating, and the dependence of the fusion $Q$ on heating power is illustrated in Sec. III B. The effects of sawtooth oscillations are described in Sec. III C. The dependence of the fusion $Q$ on pedestal temperature is shown in Sec. III D, and results are presented in Sec. III E for simulations where the toroidal momentum equation is solved using the toroidal momentum diffusivity $\chi_{\phi,\mathrm{GLF23}}$, computed using the GLF23 model in contrast to simply setting $\chi_\phi$ equal to the ion thermal diffusivity $\chi_i$.

### A. Plasma profiles and fusion power

The procedure described in Sec. II is applied to carry out ITER simulations using either the MMM95 or GLF23 model for anomalous transport and with either 30 MW of ICRF or 30 MW of NBI heating power. In the simulations with ICRF heating, the frequency is set equal to 53 MHz. In the simulations with NBI heating, the 1 MeV deuterium neutral beams are aimed 0.4 m above the plasma midplane. The toroidal rotation frequency is computed using $\chi_\phi = \chi_i$. The self-consistent computation of heat sources and heat fluxes leads to predictions for $T_e$, $T_i$, and fusion $Q$ which depend on the heating source and the anomalous transport model used. For the same auxiliary heating source, simulations using the MMM95 model yield higher central electron and ion temperatures and a higher fusion yield $Q$ than the corresponding simulations carried out using the GLF23 model.

Two simulations, one using the GLF23 model and the other using the MMM95 model, are carried out with 30 MW NBI heating. The electron temperature, ion temperature, and toroidal rotation frequency at $t=500$ s are shown in Fig. 2 as a function of $\rho$, the normalized square root of toroidal flux. The profiles computed by the simulation using GLF23 are plotted as solid lines, and the profiles computed in the simulations using MMM95 are plotted as dashed lines. The pedestal region can be seen in the outer 5% of the temperature profiles. The predicted pedestal temperature is 2.7 keV, and the predicted pedestal width is 0.05 m. It is observed that the GLF23 model yields temperature profiles that are slightly flatter in the outer 30% of the plasmas due to greater stiffness of the GLF23 model compared with the MMM95 model. The corresponding simulation with the MMM95 model yields higher central temperatures and, consequently, a higher fusion $Q$. The injected neutral beam drives a modest toroidal rotation, with a central rotation frequency close to 10 krad/s. The evolution of the central rotation frequency $\omega_{\phi 0}$ is shown in Fig. 3 for the same two NBI simulations carried out with the GLF23 and MMM95 models. The curves are smoothed to remove noise due to sawtooth oscillations. The sudden increases in $\omega_{\phi 0}$ at $t=50$ s and at $t=100$ s correspond to increases in NBI power. The rotation frequency reaches steady state soon after the end of the density ramp at 150 s. The toroidal Mach number at the magnetic axis, given by

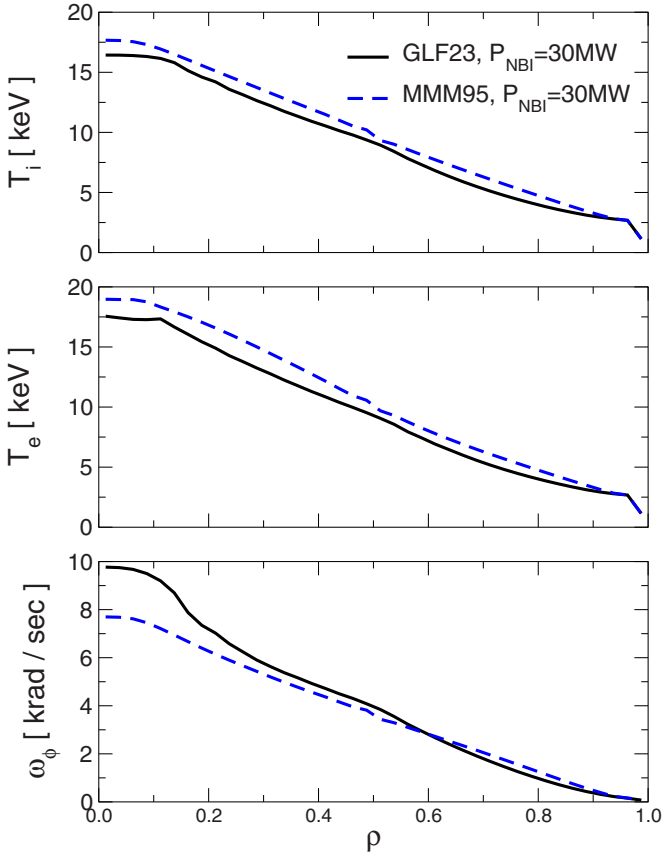


FIG. 2. (Color online) $T_e$, $T_i$, and $\omega_\phi$ profiles are shown as a function of $\rho$ for simulations using GLF23 (solid line) or MMM95 (dashed line) at $t=500$ s. The simulations were carried out using 30 MW of NBI heating.

$$\mathrm{M}_{\phi 0} = \frac{\omega_{\phi 0} R}{\sqrt{Z_{\mathrm{eff}} k_B T_{e0}/m_i}}, \tag{8}$$

is close to 5%. The time evolution of the produced fusion power $P_{\mathrm{DT}}$ is shown in Fig. 4 for simulations carried out using GLF23 with 30 MW of ICRF heating (dashed line), GLF23 with 30 MW of NBI heating (dash-dotted line), MMM95 with 30 MW of ICRF heating (solid line), and MMM95 with 30 MW of NBI heating (dotted line). The

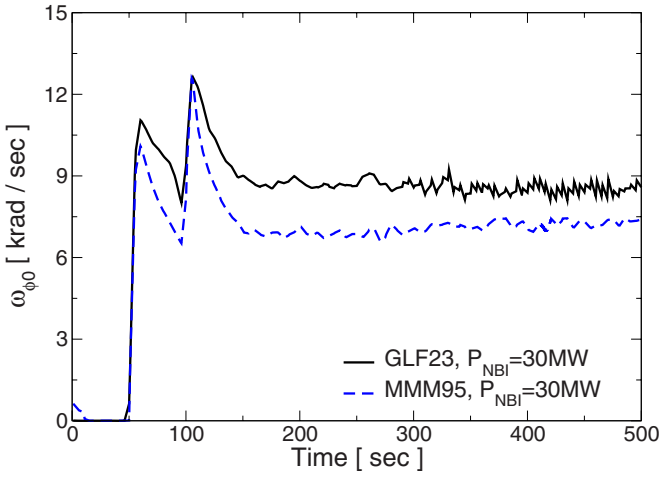


FIG. 3. (Color online) Central rotation frequency $\omega_{\phi 0}$ is shown as a function of time for simulations using GLF23 (solid line) and MMM95 (dashed line). The simulations were carried out using 30 MW of NBI heating.

curves have been smoothed to remove noise caused by sawtooth oscillations. Starting at $t=50$ s, 5 MW of auxiliary heating power is injected, and then at $t=100$ s the auxiliary heating power is increased to 30 MW. The transition from L-mode to H-mode occurs at about $t=55$ s in these simulations. The alpha heating power increases rapidly between 50 s and 150 s, while the density is still increasing. After 150 s, $P_{DT}$ increases more slowly in simulations in which the GLF23 anomalous transport model is used than in those in which MMM95 is used. This effect is probably due to stiffness of the GLF23 model; i.e., the GLF23 model responds more slowly to changes in the heating profiles than does the MMM95 model. The GLF23 simulations reach steady state around 400 s. The fusion $Q$'s, averaged between 480 and 500 s, in the simulations carried out using the GLF23 model are 8.7 for the NBI heated plasma and 7.5 for the ICRF heated plasma. The simulations carried out using MMM95 model reach steady state around $t=300$ s and result in a fusion $Q=10.4$ for both the NBI heated plasma and for the ICRF heated plasmas. The MMM95 simulation results using PTRANSP are similar to corresponding BALDUR simulation results reported in Ref. 1.

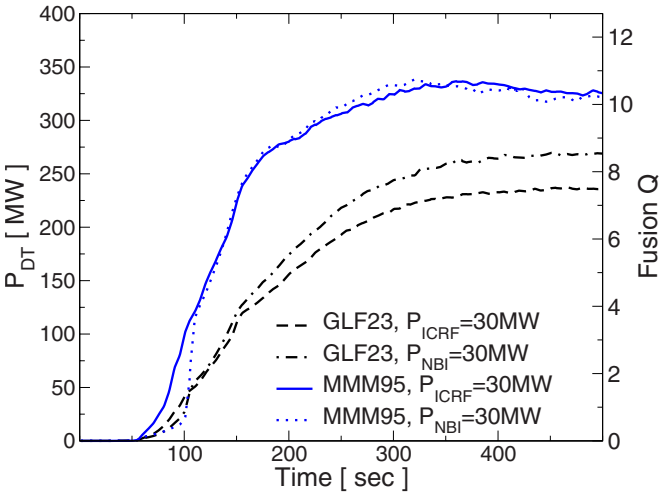


FIG. 4. (Color online) Fusion power $P_{DT}$ is shown as a function of time for simulations using: GLF23 with 30 MW of ICRF heating (dashed line) attaining a fusion $Q=7.5$; GLF23 with 30 MW of NBI heating (dashed-dotted line) attaining a fusion $Q=8.7$; MMM95 with 30 MW of ICRF heating (solid line) attaining a fusion $Q=10.4$; and MMM95 with 30 MW of NBI heating (dotted line) also attaining a fusion $Q=10.4$.

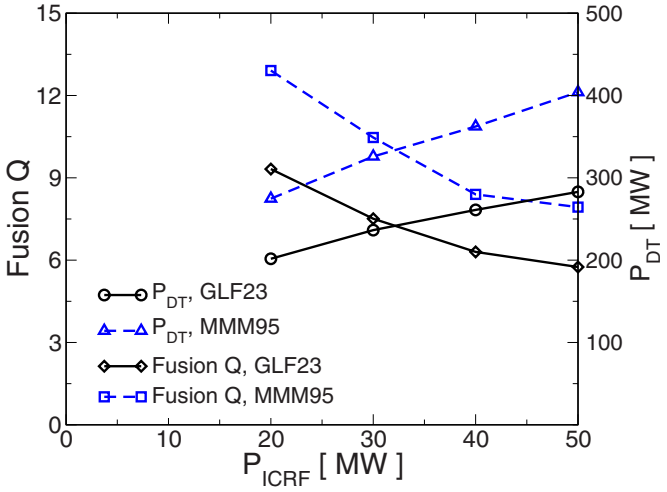


FIG. 5. (Color online) Fusion $Q$ (scale on left side) and fusion power $P_{DT}$ (scale on right side) are shown as a function of ICRF power. For the ITER simulations carried out using the GLF23 model, $Q$ is plotted as a solid line with diamonds and $P_{DT}$ is plotted as a solid line with circles. For the ITER simulations carried out using the MMM95 model, $Q$ is plotted as a dashed line with squares and $P_{DT}$ is plotted as a dashed line with triangles. The simulations are carried out using the computed pedestal temperature: $T_{ped}=2.7$ keV.

### B. Dependence of fusion *Q* on level and type of auxiliary heating power

In this subsection, the dependence of fusion $Q$ on the level and on the mix of ICRF and NBI power is examined. Although the ITER fusion power $P_{DT}$ increases with increasing input heating power, it is found that the fusion $Q$ decreases with increasing heating power. This effect is illustrated in simulations carried out with 20, 30, 40, and 50 MW of ICRF power using the predicted pedestal temperature (2.7 keV) and using the GLF23 and the MMM95 transport models. The results of these simulations are presented in Fig. 5, where the fusion $Q$ and the fusion power obtained in the simulations are shown. The solid line with diamonds represents $Q$ in simulations using GLF23, the solid line with circles represents $P_{DT}$ in simulations using GLF23, the dashed line with squares represents $Q$ in simulations using MMM95, and the dashed line with triangles represents $P_{DT}$ in simulations using MMM95. It is observed that ITER simulations using the MMM95 model with $T_{ped}=2.7$ keV and ICRF auxiliary heating predict more fusion power and a larger fusion $Q$ than in similar simulations using the GLF23 model. In both cases, however, the fusion $Q$ decreases with increasing auxiliary heating power because of the stiffness of the turbulence driven transport models.

In Fig. 4, it is shown that the fusion $Q$ obtained in the simulations depends on whether ICRF heating or NBI heating is used. For instance, a GLF23 simulation with 30 MW

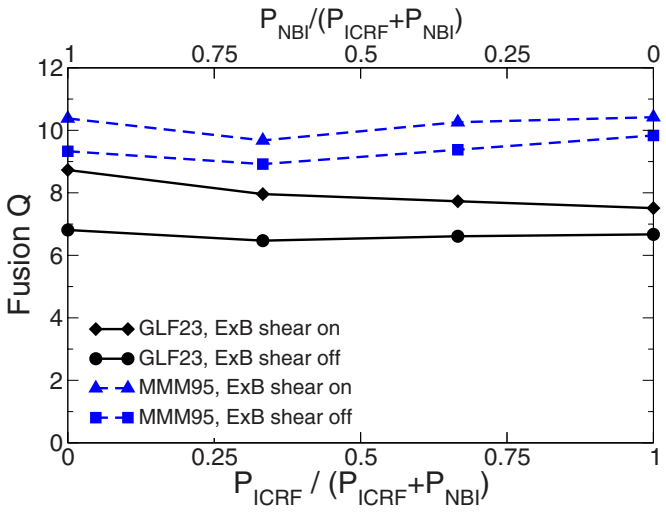


FIG. 6. (Color online) Fusion $Q$ shown for ITER simulations with a fixed total power $P_{\mathrm{Tot}}=P_{\mathrm{NBI}}+P_{\mathrm{ICRF}}=30$ MW, but using different mixes of ICRF and NBI power: $P_{\mathrm{ICRF}}/P_{\mathrm{Tot}}$. The simulations were carried out with the computed pedestal temperature, i.e., $T_{\mathrm{ped}}=2.7$ keV, using GLF23 with $\mathbf{E}\times\mathbf{B}$ flow shear on (solid line with diamonds), GLF23 with $\mathbf{E}\times\mathbf{B}$ flow shear off (solid line with circles), MMM95 with $\mathbf{E}\times\mathbf{B}$ flow shear on (dashed line with triangles), and MMM95 with $\mathbf{E}\times\mathbf{B}$ flow shear off (dashed line with squares).

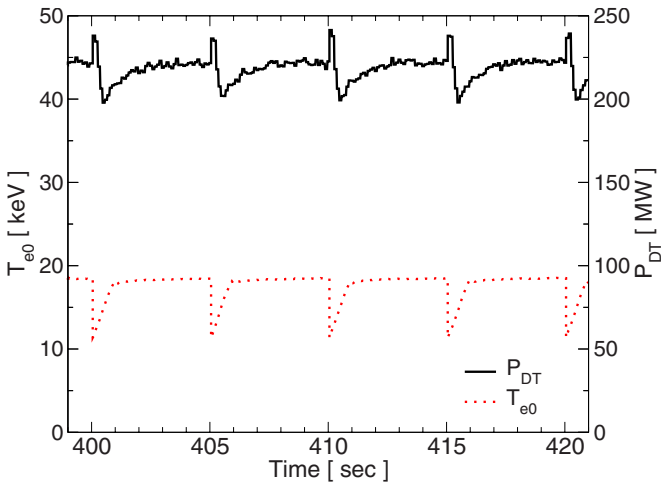


FIG. 7. (Color online) Fusion power (solid line) and central electron temperature (dashed line) are shown as a function of time to illustrate the effects of five sawtooth crashes between 399 and 421 s. The simulation was carried out with the GLF23 model and 20 MW of ICRF power at 45 MHz.

of ICRF power yields $Q=7.5$, while a GLF23 simulation with 30 MW of NBI power yields $Q=8.7$. A possible cause for this increase in fusion $Q$ is that the toroidal rotation driven by the neutral beams increases the $\mathbf{E}\times\mathbf{B}$ flow shear rate, which then decreases the turbulence driven transport. To test this hypothesis, ITER simulations are carried out with a fixed auxiliary heating power, i.e., $P_{\mathrm{Tot}}=P_{\mathrm{ICRF}}+P_{\mathrm{NBI}}=30$ MW, but with different mixes of ICRF and NBI power. Furthermore, the simulations are carried out with and without $\mathbf{E}\times\mathbf{B}$ flow shear stabilization. Note that the GLF23 model uses the flux-surface averaged $\mathbf{E}\times\mathbf{B}$ flow shear rate, which can be larger than the $\mathbf{E}\times\mathbf{B}$ shear rate at the outboard midplane that is used in the MMM95 model. Consequently, it is expected that in the GLF23 model the effect of flow shear stabilization is stronger than in the MMM95 model. The fusion $Q$ obtained in these simulations is shown in Fig. 6. The solid lines represent simulations using GLF23 with $\mathbf{E}\times\mathbf{B}$ shear stabilization (solid lines with diamonds) and without $\mathbf{E}\times\mathbf{B}$ shear stabilization (solid lines with circles), while the dashed lines represent simulations using MMM95 with $\mathbf{E}\times\mathbf{B}$ shear stabilization (dashed lines with triangles) and without $\mathbf{E}\times\mathbf{B}$ shear stabilization (dashed lines with squares). The leftmost points in the figure represent simulations using only NBI heating, while the rightmost points in the figure represent simulations using only ICRF heating. It can be seen in Fig. 6 that, for simulations using GLF23, the $\mathbf{E}\times\mathbf{B}$ shear stabilization decreases as the beam power is decreased. For simulations using MMM95, however, the $\mathbf{E}\times\mathbf{B}$ shear stabilization is found to be about the same for all the power mixes. In simulations with only NBI heating, it is found that the flow shear rates are dominated by the toroidal rotation. The poloidal rotation velocity, which is computed using the NCLASS code, is included in the calculation of the flow shear rates. Overall, due to the low toroidal rotation velocity, the dependence of the fusion gain on the fraction of NBI power in these simulations is weak.

Simulations are also carried out using the combination of ICRF and NBI power that is consistent with heating sources currently planned for ITER; that is, 20 MW of ICRF and 16.5 MW of NBI power. In addition, beam steering is utilized in the simulations to aim the neutral beam 0.4 m above the midplane, 0.1 m above the midplane, and 0.2 m below the midplane. The simulations carried out using GLF23 yield fusion $Q\approx 6.8$ and $P_{\mathrm{DT}}\approx 255$ MW, while the simulations carried out using MMM95 yield fusion $Q\approx 9.8$ and $P_{\mathrm{DT}}\approx 360$ MW. The temperature profiles are found to be insensitive to the beam steering, but the central toroidal rotation frequency is highest when the beam is aimed 0.4 m above the midplane. In simulations using GLF23, it is found that central toroidal rotation frequency is $\omega_{\phi 0}=3.94$ krad/s when the beam is aimed 0.4 m above the midplane, while $\omega_{\phi 0}=2.55$ krad/s when the beam is aimed 0.2 m below the midplane.

### C. Effect of sawtooth oscillations

In order to investigate the dependence of simulation results on the period of sawtooth oscillations, ITER simulations are carried out using sawtooth periods of 2 and 10 s. The sawtooth crash amplitude, during the quasisteady-state stage of the discharge, is found to be approximately 7 keV, independent of the sawtooth period, while the sawtooth mixing radius is found to be close to 40% of the plasma radius. The quasisteady-state fusion $Q$ and temperature obtained are not affected by the change in sawtooth period. Transients in the profiles due to sawtooth mixing are observed after every crash. The evolution of the fusion heating power production and the central electron temperature $T_{e0}$, through a few sawtooth cycles, is illustrated in Fig. 7. In this ITER simulation, the GLF23 model is used with 20 MW of ICRF power at 45 MHz. The solid line represents $P_{\mathrm{DT}}$, while the dashed line represents the central temperature. The periodic transient increases in $P_{\mathrm{DT}}$ are due to the sudden depletion of the central

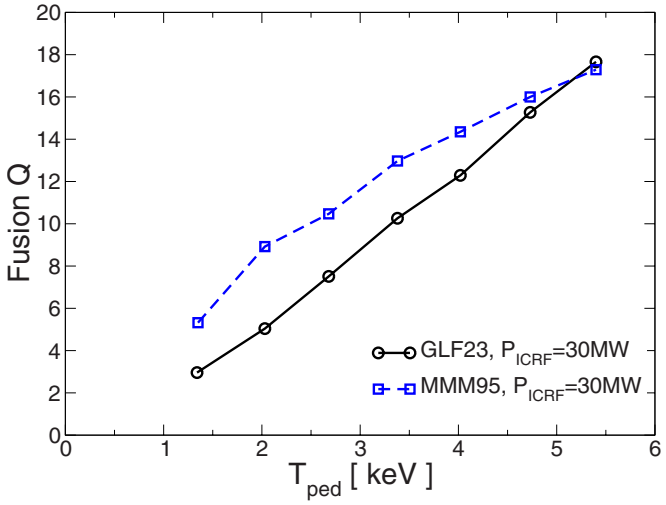


FIG. 8. (Color online) Fusion $Q$ is shown as a function of pedestal temperature for ITER simulations using GLF23 (solid line with circles) or MMM95 (dashed line with squares). The simulations were carried out using 30 MW of ICRF power.

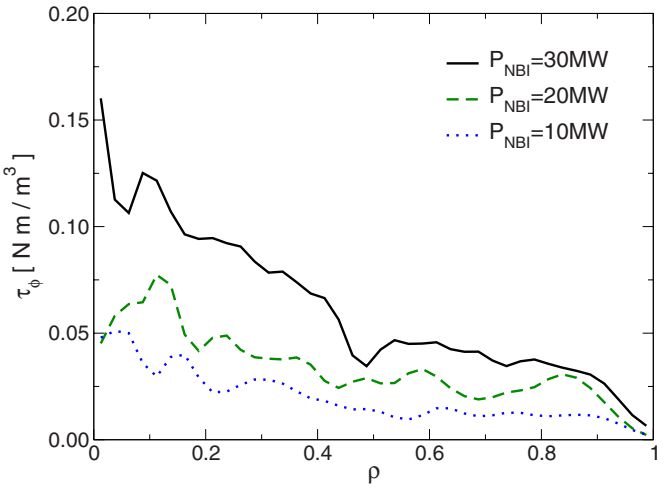


FIG. 9. (Color online) Toroidal torque profiles are shown as a function of $\rho$ for ITER simulations carried out using $P_{\mathrm{NBI}}=30$ MW (solid line), $P_{\mathrm{NBI}}=20$ MW (dashed line), and $P_{\mathrm{NBI}}=10$ MW (dotted line). The toroidal momentum transport equation is solved using the GLF23 toroidal momentum diffusivity in simulations with $T_{\mathrm{ped}}=2.7$ keV.

helium ash density after each sawtooth crash. Although the sawtooth crashes periodically affect the distribution of helium ash, the plasma profiles recover very rapidly (in about 1 s), as shown in Fig. 7. Thus, the sawtooth oscillations reach a saturated level even with a 2 s sawtooth period.

### D. Variation of fusion *Q* with pedestal temperature

The fusion $Q$ predicted for ITER depends sensitively on the temperature at the top of the H-mode pedestal. In order to illustrate this dependence, ITER simulations with 30 MW of ICRF heating are carried out using pedestal temperatures ranging from 1.35 keV (half the predicted pedestal temperature of 2.7 keV) to 5.4 keV (twice the predicted temperature). The pedestal width remains at 0.05 m, as in the rest of the simulations presented in this paper. Values of the fusion $Q$ for these simulations are shown in Fig. 8. The solid line with circles represents results from simulations carried out with the GLF23 model, while the dashed line with squares represents results from simulations carried out with the MMM95 model. Overall, the fusion $Q$ varies between $Q=2.5$ with $T_{\mathrm{ped}}=1.35$ keV (using GLF23) and $Q\approx 18$ with $T_{\mathrm{ped}}=5.4$ keV using either MMM95 or GLF23. In simulations using GLF23, it is found that $Q$ is nearly proportional to the pedestal temperature, while in simulations using MMM95 there is a more rapid increase in $Q$ at low pedestal temperature, and then a slower increase for $3.4\ \mathrm{keV}<T_{\mathrm{ped}}<5.4$ keV. The MMM95 model yields higher values of $Q$ at all pedestal temperatures below $T_{\mathrm{ped}}=5.4$ keV. Note that the difference between the GLF23 and MMM95 results is greatest in the vicinity of the predicted pedestal temperature of 2.7 keV.

### E. Toroidal momentum transport predictions using the GLF23 model

In the previous sections, the ITER simulations presented are carried out using a toroidal momentum diffusivity $\chi_\phi$ equal to the ion thermal diffusivity; i.e., $\chi_\phi=\chi_i$. In present day tokamak discharges, however, it is found that the ratio $\chi_\phi/\chi_i$, known as the Prandtl number, is between 0.2 and 0.5 (see, for example, Ref. 34). Consequently, the rotation estimates shown in Sec. III A underestimate the toroidal rotation that contributes to $\mathbf{E}\times\mathbf{B}$ flow shear turbulence stabilization.

In this section, the ITER toroidal rotation profile is computed in simulations where the toroidal momentum transport equation is evolved using the GLF23 toroidal momentum diffusivity: $\chi_{\phi,\mathrm{GLF23}}$. A neoclassical contribution, which is taken to be equal to the neoclassical ion heat diffusivity, $\chi_{i,\mathrm{NCLASS}}$, is added to $\chi_{\phi,\mathrm{GLF23}}$ to compute the toroidal momentum diffusivity

$$\chi_\phi=\chi_{\phi,\mathrm{GLF23}}+\chi_{i,\mathrm{NCLASS}}. \tag{9}$$

Since the toroidal rotation is driven by the neutral beams, the total torque input increases as the NBI power is increased. In Fig. 9, the toroidal torque density profiles are shown for ITER simulations using 30 MW (solid line), 20 MW (dashed line), and 10 MW (dotted line) of neutral beam heating. Note that, as with power deposition profiles, the volume elements are larger at larger minor radii. It is found that, although the torque profiles are not peaked, there is a significant torque component within the inner 20% of the plasma, where the volume elements are smaller. The toroidal rotation frequency profiles in simulations with 30 MW (solid line), 20 MW (dashed line), and 10 MW (dotted line) of NBI heating power are shown in Fig. 10. These profiles indicate that there is a large gradient in the rotation frequency profile just below $\rho=0.5$, and the central rotation frequency is proportional to the injected NBI power. In addition, at $P_{\mathrm{NBI}}=30$ MW the central rotation frequency $\omega_{\phi 0}$ obtained in these ITER simulations is in the same order of magnitude as $\omega_{\phi 0}$ obtained in

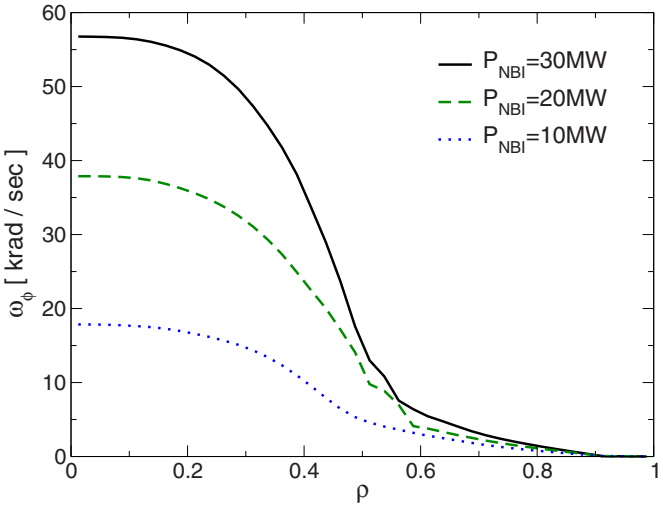


FIG. 10. (Color online) Toroidal rotation frequency profiles are shown as a function of $\rho$ for ITER simulations carried out using $P_{\mathrm{NBI}}=30$ MW (solid line), $P_{\mathrm{NBI}}=20$ MW (dashed line), and $P_{\mathrm{NBI}}=10$ MW (dotted line). The toroidal momentum transport equation is solved using the GLF23 toroidal momentum diffusivity in simulations with $T_{\mathrm{ped}}=2.7$ keV.

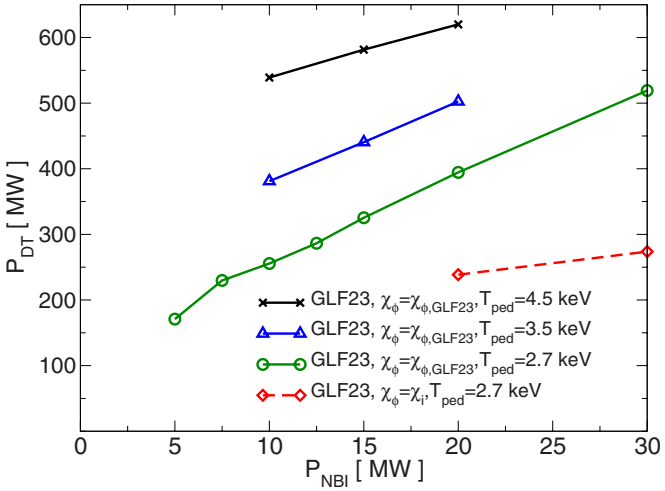


FIG. 11. (Color online) Fusion power $P_{\mathrm{DT}}$ is shown as a function of NBI power for ITER simulations where the GLF23 toroidal momentum diffusivity is used to solve the toroidal momentum transport equation. The simulations are carried out at $T_{\mathrm{ped}}=4.5$ keV (solid line with crosses), $T_{\mathrm{ped}}=3.5$ keV (solid line with triangles), and $T_{\mathrm{ped}}=2.7$ keV (solid line with circles). Simulations carried out with $\chi_\phi=\chi_i$ and with $T_{\mathrm{ped}}=2.7$ keV (dashed line with diamonds) are shown for comparison.

JET discharges with similar density but less NBI power (see, for example, Ref. 34). The Prandtl number $\chi_\phi/\chi_i$ for these ITER simulations is computed to be between 0.2 and 0.5, which is within the experimentally inferred range of values for high density JET discharges reported in Ref. 34. The GLF23 toroidal momentum diffusivity is found to be larger at the plasma edge and smaller in the deep core. For $\rho<0.4$, GLF23 predicts $\chi_\phi=0$, which means that the toroidal rotation in the plasma core is associated with only the neoclassical ion heat diffusivity.

The gradient in rotation velocity profile close to $\rho=0.5$ drives $\mathbf{E}\times\mathbf{B}$ flow shear stabilization that is much stronger in these simulations than in the corresponding simulations shown in previous sections. Because the toroidal momentum diffusivity is partially quenched by the flow shear, the plasma spins up even faster than it would without flow shear stabilization. That is, flow shear stabilization and the toroidal momentum rotation form a feedback loop.[35] In addition, the higher core plasma temperatures resulting from the increased flow shear produces an increased level of fusion power. This effect results in a further increase in the temperature, which drives the diamagnetic term of the radial electric field. Together, the changes in $\chi_\phi$, the flow shear rate, and the fusion power $P_{\mathrm{DT}}$ constitute a delicate and powerful feedback loop that is unique to burning plasmas and that is not found in present day experiments.

In Fig. 11, the fusion power production $P_{\mathrm{DT}}$ is shown as a function of NBI power for ITER simulations carried out with $T_{\mathrm{ped}}=4.5$ keV (solid line with crosses), $T_{\mathrm{ped}}=3.5$ keV (solid line with triangles), and $T_{\mathrm{ped}}=2.7$ keV (solid line with circles) with $\chi_\phi$ given by Eq. (9). For comparison, simulations carried out at $T_{\mathrm{ped}}=2.7$ keV and $\chi_\phi=\chi_i$ are shown in the plot as a dashed line. Due to the feedback effect, described above, the values of fusion $Q$ and $P_{\mathrm{DT}}$ obtained in these simulations are rather high compared to corresponding simulations shown in the previous sections (shown with the dashed line in Fig. 11). In the simulations in which the GLF23 toroidal momentum diffusivity is used, only 7.5 MW of NBI power is necessary to achieve an L-mode to H-mode transition, with the remainder of power necessary to reach the power threshold [given in Eq. (6)] provided by self-heating due to fusion reactions. A fusion power production of $P_{\mathrm{DT}}=500$ MW is obtained in the simulation with $P_{\mathrm{NBI}}=20$ MW and $T_{\mathrm{ped}}=3.5$ keV.

A similar enhancement of ITER fusion performance was found in XPTOR simulations shown in Ref. 7. In that paper, it was found that $P_{\mathrm{DT}}\approx 300$ MW at $T_{\mathrm{ped}}=3.5$ keV and $P_{\mathrm{DT}}\approx 440$ MW at $T_{\mathrm{ped}}=4.5$ keV, while in the present work we find $P_{\mathrm{DT}}\approx 380$ MW at $T_{\mathrm{ped}}=3.5$ keV and $P_{\mathrm{DT}}\approx 540$ MW at $T_{\mathrm{ped}}=4.5$ keV. A sharp increase in fusion power due to the formation of an internal transport barrier is found in Ref. 7 for more than 10 MW of NBI power. In the present study, a similar transport barrier is not found with the levels of auxiliary heating power considered.

Note that the improvement of fusion power production, which results from shearing rates inside $\rho<0.5$, is not supported by existing experimental data. The improvement of confinement could be overestimated in the simulations. This sensitivity to flow shear in the GLF23 model is because the growth rates of the ITG/TEM instability are comparable to the $\mathbf{E}\times\mathbf{B}$ flow shear rates. Consequently, a small increase in the flow shear rates can have a large impact on fusion power production. The strength of the feedback loop between thermal transport and toroidal rotation would be reduced in other models where the growth rate of the ITG/TEM instability is larger. Results shown in previous subsections with the MMM95 and GLF23 transport models hint at this difference between the sensitivity of the models to flow shear.

## IV. SUMMARY AND CONCLUSIONS

In this paper, the PTRANSP code is utilized to compute fusion power scenarios for 15 MA H-mode ITER discharges. Two models for turbulent transport are used with several choices for the edge pedestal temperature and with different choices for auxiliary heating source and power levels. The NBI, ICRF, and alpha power sources are computed self-consistently together with the plasma temperature, the current density profile, and the build-up of helium ash.

The toroidal rotation is computed by balancing the NBI sources of torque with anomalous momentum diffusivity $\chi_\phi$. When $\chi_\phi$ is taken to be equal to the ion thermal diffusivity, i.e., $\chi_\phi=\chi_i$, the resulting toroidal rotation frequency is rather modest, and the toroidal Mach number is about $M_\phi \approx 0.05$. However, when the GLF23 model is used to compute the anomalous momentum diffusivity $\chi_{\phi,\mathrm{GLF23}}$, the flow shear effect is more significant.

It was found in the simulations carried out that the balance between heat fluxes and heat sources evolves slowly. The alpha heating power rises from 50 s until about 300 s. At that time, the evolution of the current profile and the build-up of helium ash stabilize to quasisteady-state conditions. The evolution of the current profile is affected by the beam driven current, which depends on the core plasma temperature profiles, as well as on the bootstrap current driven in the edge pedestal region. With the PEDESTAL module temperature equal to 2.7 keV and using the GLF23 anomalous transport model, PTRANSP simulations yield a fusion $Q$ equal to 7.5 with ICRF heating and 8.9 with NBI heating, while simulations using the MMM95 model yield a fusion $Q$ equal to 10.4 for both heating sources. These predictions for $Q$ are similar to those previously found using the BALDUR code and the XPTOR code. However, in the BALDUR and XPTOR simulations the input (auxiliary) heating profiles were prescribed and, thus, did not respond to changes in the temperature profiles due to the fusion power. In addition, in the XPTOR code the current profile is not evolved. In view of these differences, the levels of agreement between the simulation results in Sec. III A and the corresponding BALDUR and XPTOR results are rather good.

The dependence of fusion $Q$ and $P_{\mathrm{DT}}$ with respect to the auxiliary heating power is studied by carrying out simulations with 20, 30, 40, and 50 MW of ICRF power. For these simulations, ICRF power is chosen in order to study the scaling of $Q$ with input power independent of the effect that $\mathbf{E}\times\mathbf{B}$ flow shear stabilization associated with NBI would have on $Q$. It is found that the fusion power production increases slowly with additional ICRF power and, consequently, the fusion $Q$ decreases with increasing ICRF power. It is also found that a higher fusion $Q$ is obtained using the MMM95 model than is obtained in corresponding simulations using the GLF23 model.

The influence of the $\mathbf{E}\times\mathbf{B}$ flow shear is studied by carrying out simulations with and without $\mathbf{E}\times\mathbf{B}$ flow shear at a fixed auxiliary power $P=P_{\mathrm{ICRF}}+P_{\mathrm{NBI}}=30$ MW, but with the fraction of NBI and ICRF power varied. In simulations carried out using the GLF23 model, it is found that the fusion $Q$ increases as the fraction of NBI power increases, although the diamagnetic flow drives some flow shear stabilization even when all of the heating power is due to ICRF. In simulations carried out using the MMM95 model, it is found that the flow shear stabilization does not increase significantly as the beam power is increased.

In a scenario in which 20 MW of ICRF power and 16.5 of NBI power were applied (as currently planned in the ITER design), the neutral beam was aimed, successively, 0.4 m above the midplane, 0.1 m above the midplane, and 0.2 m below the midplane. Although the computed fusion power produced varies minimally with the steering of the beams in these simulations, it is observed that the rotation velocity decreases when the beam is aimed 20 cm below the midplane. With the application of 20 MW of ICRF power and 16.5 MW of NBI power, simulations using the GLF23 model yield $Q=6.8$ and $P_{\mathrm{DT}}=255$ MW, while comparable simulations using the MMM95 model yield $Q=9.8$ and $P_{\mathrm{DT}}=360$ MW.

Sawtooth oscillations, which periodically mix the central plasma profiles, are found to alter the plasma equilibrium profiles and $P_{\mathrm{DT}}$ only immediately after each sawtooth crash. The periodic transient increases in fusion power are found to be due to the sudden depletion of helium ash caused by each sawtooth crashes. After each sawtooth crash, the plasma profiles recover in about 1 s. Thus, even with a sawtooth period as short as 2 s, the sawtooth crashes occur at full amplitude.

The height of the edge H-mode pedestal strongly influences the fusion performance of ITER. Simulations are carried out using $1.35<T_{\mathrm{ped}}<5.4$ (with 30 MW of ICRF input power). In these simulations, the fusion $Q$ varies between 3 and 18. The value of $Q$ is nearly proportional to $T_{\mathrm{ped}}$ when the GLF23 model is used, which is plausibly due to thermal transport stiffness and the resulting temperature profile stiffness. In simulations using MMM95, $Q$ scales more modestly as the pedestal temperature increases.

The GLF23 toroidal momentum diffusivity is used, together with a neoclassical enhancement, to evolve the toroidal momentum transport equation self-consistently together with thermal transport, flow shear stabilization, and the neutral beam source. ITER simulations using the GLF23 predicted momentum diffusivity were carried out with NBI heating powers between 5 and 30 MW. It is found that the Prandtl number is in the range $0.2<\chi_{\phi,\mathrm{GLF23}}/\chi_i<0.5$, which is in agreement with inferred values obtained from present day experiments. In the inner 40% of the plasma, momentum transport is dominated by the neoclassical addition, which is the weakest element in the model. (It has been predicted that the neoclassical toroidal momentum diffusivity is much smaller than the neoclassical ion heat diffusivity.) In simulations using $\chi_{\phi,\mathrm{GLF23}}+\chi_{i,\mathrm{NCLASS}}$, the predicted central toroidal rotation frequency is found to be proportional to the injected NBI power. At 30 MW of NBI power, the central toroidal rotation frequency is $\omega_{\phi 0}=57$ krad/s (shown in Fig. 10), which is approximately six times larger than the frequency predicted using $\chi_\phi=\chi_i$ (shown in Fig. 2). A large gradient in rotation velocity is found in the simulations due to the small toroidal momentum transport predicted by the GLF23 model. When the toroidal momentum diffusivity is computed using the GLF23 model, a strong toroidal velocity gradient results

in strong stabilization of thermal transport and enhanced production of fusion power relative to simulations in which $\chi_\phi = \chi_i$.

## ACKNOWLEDGMENTS

We thank the U.S. DOE for supporting this research under Contract Nos. DE-FG02-92ER54141 and DE-AC02-76-CHO3073.

[1] G. Bateman, T. Onjun, and A. H. Kritz, Plasma Phys. Controlled Fusion **45**, 1939 (2003).
[2] J. E. Kinsey, G. Bateman, T. Onjun, A. H. Kritz, A. Pankin, G. M. Staebler, and R. E. Waltz, Nucl. Fusion **43**, 1845 (2003).
[3] V. Mukhovatov, Y. Shimomura, A. Polevoi, M. Shimada, M. Sugihara, G. Bateman, J. Cordey, O. Kardaun, G. Pereverzev, I. Voitsekhovich, J. Weiland, O. Zolotukhin, A. Chudnovskiy, A. Kritz, A. Kukushkin, T. Onjun, A. Pankin, and F. Perkins, Nucl. Fusion **43**, 942 (2003).
[4] T. Onjun, A. H. Kritz, G. Bateman, and V. Parail, Phys. Plasmas **12**, 082513 (2005).
[5] J. E. Kinsey, G. M. Staebler, and R. E. Waltz, Phys. Plasmas **12**, 052503 (2005).
[6] W. Houlberg, C. Gormezano, J. Artaud, E. Barbato, V. Basiuk, A. Becoulet, P. Bonoli, R. Budny, L. Eriksson, D. Farina, Y. Gribov, R. Harvey, J. Hobirk, F. Imbeaux, C. Kessel, V. Leonov, M. Murakami, A. Polevoi, E. Poli, R. Prater, H. S. John, F. Volpe, E. Westerhof, A. Zvonkov, ITPA Steady State Operation Topical Group, and ITPA Confinement Database and Modeling Topical Group, Nucl. Fusion **45**, 1309 (2005).
[7] G. M. Stabler and H. E. S. John, Nucl. Fusion **46**, L6 (2006).
[8] C. E. Kessel, G. Giruzzi, A. C. C. Sips, R. V. Budny, J. F. Artaud, V. Basiuk, F. Imbeaux, E. Joffrin, M. Schneider, M. Murakami, T. Luce, H. S. John, T. Oikawa, N. Hayashi, T. Takizuka, T. Ozeki, Y.-S. Na, J. M. Park, J. Garcia, and A. A. Tucillo, Nucl. Fusion **47**, 1274 (2007).
[9] R. V. Budny, R. Andre, G. Bateman, F. Halpern, C. E. Kessel, A. Kritz, and D. McCune, Nucl. Fusion **48**, 075005 (2008).
[10] T. A. Casper, W. H. Meyer, L. D. Pearlstein, and A. Portone, Fusion Eng. Des. **83**, 552 (2008).
[11] R. E. Waltz, G. M. Staebler, W. Dorland, G. W. Hammett, and M. Kotschenreuther, Phys. Plasmas **4**, 2482 (1997).
[12] G. Bateman, A. H. Kritz, J. E. Kinsey, A. J. Redd, and J. Weiland, Phys. Plasmas **5**, 1793 (1998).
[13] J. Weiland, *Collective Modes in Inhomogeneous Plasmas and Advanced Fluid Theory* (Institute of Physics, Bristol, 1999).
[14] M. Erba, T. Aniel, V. Basiuk, A. Becoulet, and X. Litaudon, Nucl. Fusion **38**, 1013 (1998).
[15] J. E. Kinsey, G. M. Staebler, and R. E. Waltz, Fusion Sci. Technol. **44**, 763 (2003).
[16] C. E. Singer, D. E. Post, D. R. Mikkelsen, M. H. Redi, A. McKenney, A. Silverman, F. G. P. Seidl, P. H. Rutherford, R. J. Hawryluk, W. D. Langer, L. Foote, D. B. Heifetz, W. A. Houlberg, M. H. Hughes, R. V. Jensen, G. Lister, and J. Ogden, Comput. Phys. Commun. **49**, 275 (1988).
[17] C. D. Challis, J. G. Cordey, H. Hamnen, P. M. Stubberfield, J. P. Christiansen, E. Lazzaro, D. G. Muir, D. Stork, and E. Thompson, Nucl. Fusion **29**, 563 (1989).
[18] R. J. Hawryluk, in *Physics of Plasmas Close to Thermonuclear Conditions* (Commission of the European Communities, Brussels, 1981), Vol. 1, p. 19.
[19] K. H. Burrell, Phys. Plasmas **4**, 1499 (1996).
[20] P. H. Rebut, R. J. Bickerton, and B. E. Keen, Nucl. Fusion **25**, 1011 (1985).
[21] T. Tala, Y. Andrew, K. Crombé, P. de Vries, X. Garbet, N. Hawkes, H. Nordman, K. Rantamäki, P. Strand, A. Thyagaraja, J. Weiland, E. Asp, Y. Baranov, C. Challis, G. Corrigan, A. Eriksson, C. Giroud, M.-D. Hua, I. Jenkins, H. Knoops, X. Litaudon, P. Mantica, V. Naulin, V. Parail, K.-D. Zastrow, and JET-EFDA Contributors, Nucl. Fusion **47**, 1012 (2007).
[22] F. Porcelli, D. Boucher, and M. N. Rosenbluth, Plasma Phys. Controlled Fusion **38**, 2163 (1996).
[23] L. E. Zakharov and A. Pletzer, Phys. Plasmas **6**, 4693 (1999).
[24] B. B. Kadomtsev, Sov. J. Plasma Phys. **1**, 389 (1975).
[25] W. A. Houlberg, K. C. Shaing, S. P. Hirshman, and M. C. Zarnstorff, Phys. Plasmas **4**, 3220 (1997).
[26] M. Evrard, J. Ongena, and D. V. Eester, AIP Conf. Proc. **355**, 235 (1995).
[27] R. J. Goldston, D. C. McCune, H. H. Towner, S. L. Davis, R. J. Hawryluk, and G. L. Schmidt, J. Comput. Phys. **43**, 61 (1981).
[28] A. Pankin, D. C. McCune, R. Andre, G. Bateman, and A. H. Kritz, Comput. Phys. Commun. **159**, 157 (2004).
[29] J. E. Kinsey, G. M. Staebler, and R. E. Waltz, Phys. Plasmas **9**, 1676 (2002).
[30] T. Onjun, G. Bateman, A. H. Kritz, and G. Hammett, Phys. Plasmas **9**, 5018 (2002).
[31] Y. Shimomura, Y. Murakami, A. R. Polevoi, P. Barabaschi, V. Mukhovatov, and M. Shimada, Plasma Phys. Controlled Fusion **43**, A385 (2001).
[32] E. J. Doyle, W. A. Houlberg, Y. Kamada, V. Mukhovatov, T. H. Osborne, A. Polevoi, G. Bateman, J. W. Connor, J. G. Cordey, T. Fujita, X. Garbet, T. S. Hahm, L. D. Horton, A. E. Hubbard, F. Imbeaux, F. Jenko, J. E. Kinsey, Y. Kishimoto, J. Li, T. C. Luce, Y. Martin, M. Ossipenko, V. Parail, A. Peeters, T. L. Rhodes, J. E. Rice, C. M. Roach, V. Rozhansky, F. Ryter, G. Saibene, R. Sartori, A. C. C. Sips, J. A. Snipes, M. Sugihara, E. J. Synakowski, H. Takenaga, T. Takizuka, K. Thomsen, M. R. Wade, and H. R. Wilson, Nucl. Fusion **47**(6), S18 (2007).
[33] R. J. Goldston, in *Basic Physical Processes of Toroidal Fusion Plasmas* (Commission of the European Communities, Brussels, 1986), Vol. 1, p. 165.
[34] P. C. de Vries, K. M. Rantamäki, C. Giroud, E. Asp, G. Corrigan, A. Eriksson, M. de Greef, I. Jenkins, H. C. M. Knoops, P. Mantica, H. Nordman, P. Strand, T. Tala, J. Weiland, K.-D. Zastrow, and J. E. Contributors, Plasma Phys. Controlled Fusion **48**, 1693 (2006).
[35] J. Kinsey, G. Staebler, and R. Waltz, Phys. Plasmas **9**, 1676 (2002).

The Princeton Plasma Physics Laboratory is operated
by Princeton University under contract
with the U.S. Department of Energy.

Information Services
Princeton Plasma Physics Laboratory
P.O. Box 451
Princeton, NJ 08543

Phone: 609-243-2750
Fax: 609-243-2751
e-mail: pppl_info@pppl.gov
Internet Address: http://www.pppl.gov